metals

MDPI

Article

Effect of Varying Ce Content on the Mechanical Properties and Corrosion Resistance of Low-Elastic-Modulus Mg-Zn-Ce Amorphous Alloys

Meifeng He [1], Mingming Wang [1], Ke Zhang [1], Haitao Wang [1], Hong Jiang [1] and Zhanjun Lu [2,*]

[1] School of Materials Science and Engineering, University of Shanghai for Science and Technology, Shanghai 200093, China
[2] Department of Gastroenterology, ShangHai General Hospital Jintan District Hospital, Changzhou 213200, China
* Correspondence: lzjdoctor@126.com

Abstract: Magnesium alloys have good biocompatibility because they have mechanical properties similar to those of human bones, are biodegradable, and release non-toxic corrosion products and ions in the human body. In this study, a new type of $Mg_{70-x}Zn_{30}Ce_x$ (x = 2, 4, 6, and 8) amorphous magnesium alloy was prepared by copper roller melt-spinning, and the corresponding mechanical properties and corrosion resistance were studied. The results showed that when x = 4 and 6, the Mg-Zn-Ce amorphous alloys had decent amorphous forming abilities. The addition of Ce could effectively improve the ductility of the magnesium-based amorphous alloys with an elastic modulus of each sample ranging between 30 and 58 GPa, which was similar to that of human bones; thus, these materials could effectively prevent the stress shielding effect caused by excessive elastic modulus after implantation. Additionally, the addition of an adequate amount of Ce significantly improved the corrosion resistance of the alloy. The experimental results showed that the best corrosion resistance of the magnesium-based amorphous alloys was achieved when x = 6.

Keywords: magnesium-based amorphous alloys; low elastic modulus; shear band; corrosion resistance

Citation: He, M.; Wang, M.; Zhang, K.; Wang, H.; Jiang, H.; Lu, Z. Effect of Varying Ce Content on the Mechanical Properties and Corrosion Resistance of Low-Elastic-Modulus Mg-Zn-Ce Amorphous Alloys. *Metals* **2022**, *12*, 1637. https://doi.org/10.3390/met12101637

Academic Editor: Manuel Aureliano

Received: 16 August 2022
Accepted: 21 September 2022
Published: 29 September 2022

1. Introduction

Biodegradable implant materials offer significant potential for repairing bone defects [1], as the implant materials do not need to be removed, thus preventing damage inflicted by follow-up surgeries [2–5]. Among all of the reported bone implant materials, magnesium alloys have attracted widespread attention from researchers due to their biodegradability and improved mechanical properties compared to polymer materials [6–9]. However, the biomedical applications of magnesium alloys are limited due to certain shortcomings in their properties [10]. For example, their elastic modulus is higher than that of human bone, they have a faster corrosion rate than the growth rate of human bone, and cysts can form at the implantation site due to hydrogen evolution during the corrosion process, which can adversely affect wound healing [11,12]. Therefore, research has focused on developing a new type of magnesium alloy with a low modulus, high strength, and controllable corrosion rate [13]. Amorphous alloys can more adequately meet the requirements and application standards for biomedical materials, as their special atomic structures allow different elements to dissolve with each other at larger concentrations without restricting the equilibrium phase diagram. This changes the physical and chemical properties of the alloys by adjusting the alloying elements and their fractions [14]. Compared with the crystal Mg alloys, amorphous Mg alloys [15] usually have excellent degradation resistance, and they also exhibit great potential in clinical applications [16]. Mg alloys could eliminate the stress shielding effect due to their low elastic modulus and a density similar to that of nature bone [17]. Therefore, it is imperative to study magnesium-based amorphous

alloys with excellent ductility and outstanding biocompatibility [18]. Currently no sufficient studies on magnesium-based amorphous alloys with excellent ductility have been conducted; although some studies have reported on the plastic deformation mechanisms of amorphous alloys [19], the development of degradable biomedical materials for the human body is extremely necessary [20].

Adding rare-earth elements to the alloy can effectively improve the mechanical properties and corrosion resistance of magnesium alloys [21]. Mg-based alloys containing rare-earth (RE) and transition-metal (TM) elements as solute components have attracted great interest in the field of bulk metallic glass [22,23].Rare-earth element Ce and alkaline-earth element Ca have similar physical and chemical properties, as they have similar atomic sizes and melting points, and their tensile strengths are similar to their yield strengths. In magnesium-zinc-calcium alloys, the microalloying of Ce can also enhance the corrosion resistance of the magnesium alloy [24].Therefore, in this study, Ce was used as a substitute for Ca elements in Mg-Zn-Ca magnesium-based amorphous alloys to study the effects of Ce content changes on the mechanical and corrosion properties of Mg-Zn-Ce amorphous alloys.

The research results showed that the addition of Ce elements improved the mechanical properties of the material, strengthened its corrosion resistance, and reduced the corrosion of the alloy matrix, bolstering the application prospects of the material.

2. Experiments

2.1. Material Preparation and Characterization

Pure metal Mg, Zn, and Ce (purity > 99.9%) were weighed according to the following atomic ratios: $Mg_{68}Zn_{30}Ce_2$, $Mg_{66}Zn_{30}Ce_4$, $Mg_{64}Zn_{30}Ce_6$, and $Mg_{62}Zn_{30}Ce_8$, using a high-precision balance. Then, the metals were placed in a boron nitride crucible and melted in a high-purity argon atmosphere using an induction melting furnace and subsequently cast in a copper mold. Afterward, amorphous ribbons were obtained with a thickness of 15–20 μm by using a vacuum single-roller melt-spinning device in argon. The atomic structures of the amorphous alloy ribbons were characterized by X-ray diffraction (XRD, Bruker D8 advanced diffractometer equipped with Cu- Kα radiation, Bruker Corporation, Ettlingen, Gemany). The glass transition and crystallization behavior of the obtained amorphous aoys were studied by differential scanning calorimetry (DSC, TA Q2000, NETZSCH-Gerätebau GmbH, Selb, Gemany) at a heating rate of 40 K/min. The characteristic shear bands near the fracture of the magnesium-based amorphous alloy ribbons.were studied by scanning electron microscope (SEM, Quanta 450, Thermo Fisher Scientific, Waltham, MA, USA)

2.2. Mechanical Property Testing

The load-displacement curve, elastic modulus, and microhardness of the four types of magnesium-based amorphous alloy samples were obtained using a nanoindenter. By adjusting the load, the indenter was pressed 200 nm into the sample surface at a constant rate, and the load was maintained for 10 s.

2.3. Electrochemical Property Testing

A Gamry Interface 1000 (USA) electrochemical workstation (Gamry Instruments, Warminster, PA, USA)was used for electrochemical testing. In the three-electrode system, a platinum plate was used as the counter electrode, a saturated calomel electrode was used as the reference electrode, and the Mg-Zn-Ce amorphous alloy sample served as the working electrode. The electrolyte consisted of simulated body fluid (SBF) (18.00 g/L of NaCl, 0.20 g/L of KCl, 0.20 g/L of $CaCl_2$, 1.00 g/L of $NaHCO_3$, 1.00 g/L of glucose, 0.10 g/L of $MgCl_2{\cdot}6H_2O$, and 0.05 g/L of NaH_2PO_4, pH 7.4). Each sample was initially tested for open circuit potential (OCP) for 1200 s at a scan rate of 1 mV/s. Then, electrochemical impedance spectroscopy (EIS) was carried out at a scanning frequency of 100–0.1 MHz, and finally, potentiodynamic polarization testing was performed at a scan rate of 1 mV/s.

2.4. X-ray Photoelectron Spectroscopy (XPS) Characterization

X-ray photoelectron spectroscopy (XPS, Thermo ESCALAB 250XI, Thermo Fisher Scientific, Waltham, MA, USA) was used to characterize the composition and chemical state of the passivation film. XPS measurements were obtained with a PHI 5700/660 physical electron spectrometer in an ultra-high vacuum (10^{-10} torr), using a monochromatic Al-Kα X-ray source with 1486.6 eV of energy. The XPS samples used for testing were stored in a vacuum (10^{-9} torr) for 12 h. First, the spectrum of each sample was collected with a pass energy of 187.85 eV. Then, MultiPak software (9.9.2, ULVAC-PHI, Chigasaki, Japan) was used to analyze the spectra of all of the samples based on the C1s peaks of the amorphous carbon, which accumulated on the sample surfaces, and the C1s peak was used as a reference for charge correction. All of the spectra collected during XPS analysis were measured with a pass energy of 11.75 eV and a resolution of 0.1 eV.

3. Results and Discussion

3.1. Microstructure and Thermal Properties

The atomic structures of the magnesium-based amorphous alloy with Ce content were measured by XRD, as shown in Figure 1a, and the diffraction peaks ranged from 32° to 44°. As the atomic ratio of Ce increased, peak intensity initially declined and then increased, indicating that neither reduced nor excessive addition of rare-earth elements was beneficial to the formation of amorphous structures in the system. The results showed that the prepared $Mg_{70-x}Zn_{30}Ce_x$ (x = 2, 4, 6, and 8) samples were all amorphous structures. The exothermic crystallization peaks of the samples were visible in the DSC curves, indicating that the ribbons prepared at a low Ce alloying level were amorphous, which was consistent with the XRD analysis results. As shown in Figure 1b, the sample crystallization process proceeded in multiple steps during the heating process; however, as the atomic ratio of Ce increased, the crystallization process of the sample changed from multiple steps to one step.

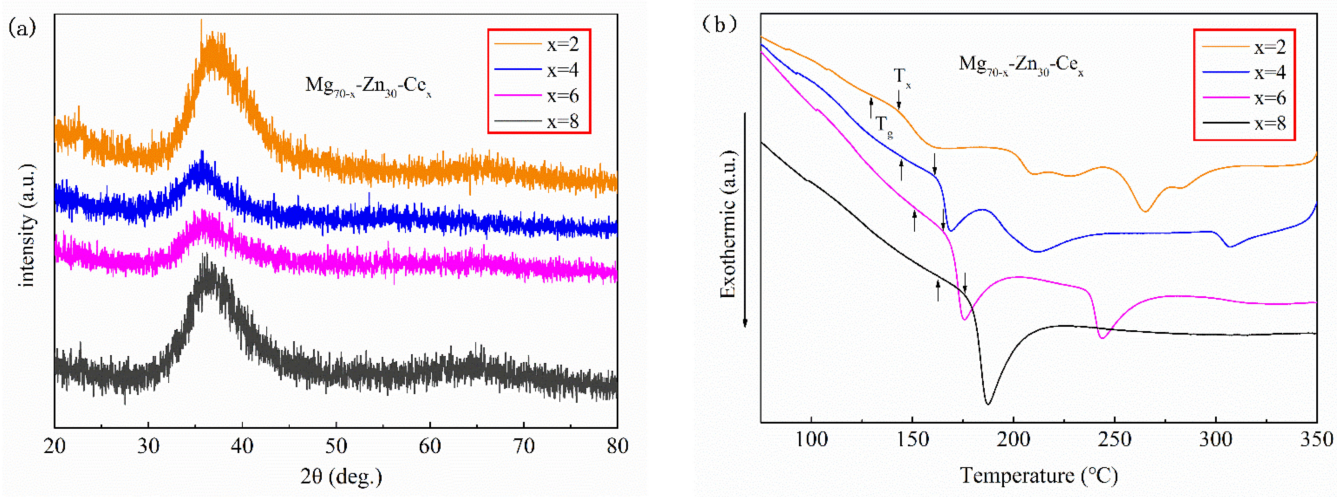

Figure 1. (**a**) XRD image of the magnesium-based amorphous alloy ribbon with Ce content, (**b**) DSC curves of the ribbons with different Ce element content.

The supercooled liquid region ΔT_x ($\Delta Tx = T_x - T_g$) was calculated by analyzing the glass transition temperature (T_g) and crystallization temperature (T_x) of the four ribbon samples ($Mg_{68}Zn_{30}Ce_2$, $Mg_{66}Zn_{30}Ce_4$, $Mg_{64}Zn_{30}Ce_6$, and $Mg_{62}Zn_{30}Ce_8$), as shown in Table 1. As Ce content increased, the values of T_g and T_x increased, and ΔT_x initially increased and then decreased. Under normal circumstances, the higher the value of ΔT_x, the better the glass forming ability (GFA) of amorphous alloys, and either reduced or excessive Ce content can lower the amorphous forming ability of an amorphous alloy system. The results in this work showed that $Mg_{66}Zn_{30}Ce_4$ had the best amorphous forming ability.

Table 1. Thermodynamic parameters of the $Mg_{70-x}Zn_{30}Ce_x$ (x = 2, 4, 6, and 8) amorphous alloys.

Alloy Composition	T_g (°C)	T_x (°C)	ΔT_x (°C)
$Mg_{68}Zn_{30}Ce_2$	129.2	143	13.8
$Mg_{66}Zn_{30}Ce_4$	144.2	160.7	16.5
$Mg_{64}Zn_{30}Ce_6$	151	165	14
$Mg_{62}Zn_{30}Ce_8$	162.6	175.5	12.9

3.2. Mechanical Properties

In this study, nanoindentation was used to measure the mechanical properties. The displacement-load curves of the four $Mg_{70-x}Zn_{30}Ce_x$ (x = 2, 4, 6, and 8) samples are shown in Figure 2a, where the shear band transition zone, which was activated when it was subjected to an external force, caused elastic atomic displacement around it, resulting in overall macroscopic strain. Each shear band was surrounded by either a micron-scale effective deformation zone or a shear-band affected zone. After the formation of the shear band, the elastic stress field redistributed and formed a progressive stress field, triggering more shear bands upon yielding [25]. The continuous propagation of the shear band and the superposition of the stress fields in the shear-band affected zone were manifested as sawtooth-shape steps in the stress-displacement curves of the four samples upon loading [26]. Figure 2b,c shows the elastic modulus and microhardness obtained by nanoindentation. With the addition of Ce elements, the elastic modulus of the sample gradually decreased, approximately to the elastic modulus of human bone, effectively averting the resulting stress shielding effect if the material was used as a bone implant. In addition, the microhardness of the sample initially decreased and then increased. A macroscopic optical image of the sample under bending is shown in Figure 2d. The $Mg_{68}Zn_{30}Ce_2$ ribbon sample, which had a mirror-like surface (thickness of about 20 μm), could be bent to 180° without breaking, exhibiting very good plasticity.

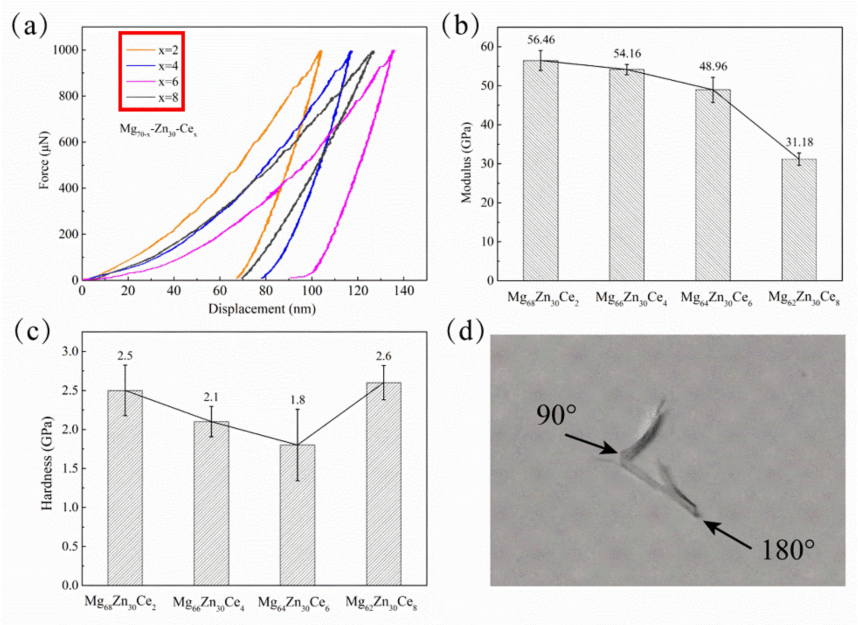

Figure 2. (**a**) Nanoindentation curves of the four samples, (**b**) elastic modulus of the four samples, (**c**) microhardness of the four samples, (**d**) optical image of the bent Ce_2 ribbon.

3.3. Microscopic Mechanism of Ductility

In this study, experimentation showed that the prepared $Mg_{68}Zn_{30}Ce_2$ and $Mg_{66}Zn_{30}Ce_4$ sample alloys exhibited good plasticity. Therefore, their fracture morphology was analyzed to study the microscopic mechanism of ductility.

Shear bands in amorphous alloys are believed to play a role similar to dislocations in crystalline alloys, as they are both the result of plastic deformation, and a large number of shear bands are found in ductile amorphous alloys after plastic deformation [27]. In the side-view images near the fracture surface of the $Mg_{68}Zn_{30}Ce_2$ and $Mg_{66}Zn_{30}Ce_4$ ribbons in Figure 3, multiple shear bands were clearly observed near the fracture. The fracture surfaces of the amorphous samples were a combination of smooth and vein pattern regions. The vein pattern is typical for amorphous alloy structures with good plasticity [28].

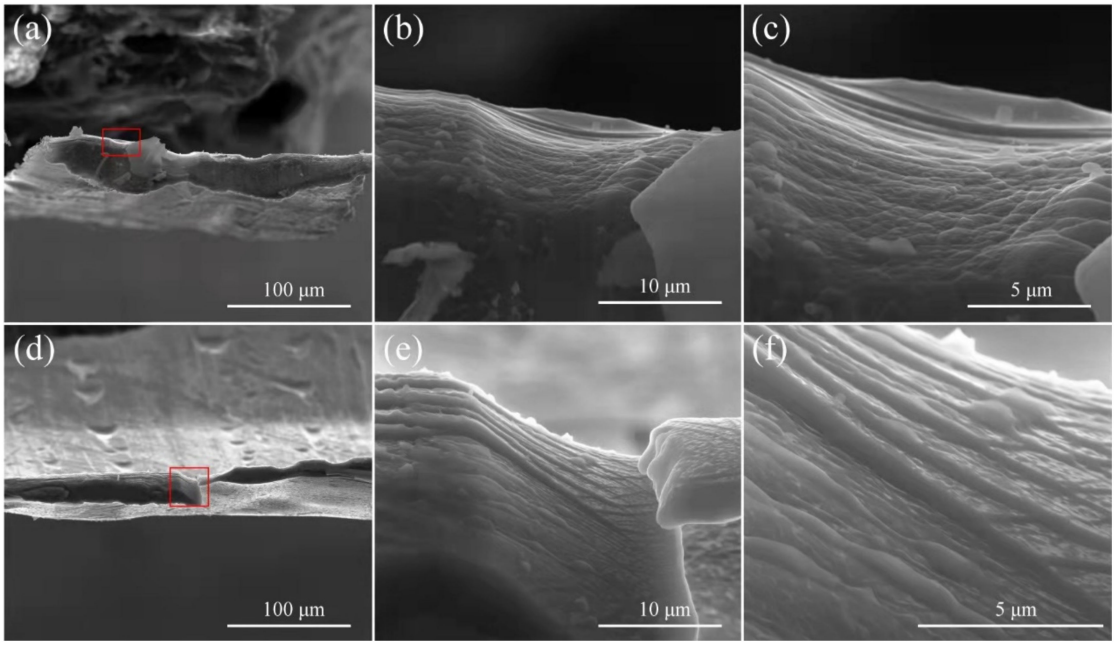

Figure 3. SEM images showing the characteristic shear bands near the fracture of the magnesium-based amorphous alloy ribbons: (**a**–**c**) $Mg_{68}Zn_{30}Ce_2$, (**d**–**f**) $Mg_{66}Zn_{30}Ce_4$.

The fracture surfaces of $Mg_{64}Zn_{30}Ce_6$ and $Mg_{62}Zn_{30}Ce_8$ are shown in Figure 4. Shear bands were sporadically present near the fracture surface of $Mg_{64}Zn_{30}Ce_6$. The shear bands near the fracture of $Mg_{62}Zn_{30}Ce_8$ were distributed more sporadically and appeared to be crystallized based on the fracture morphology, which was likely the key reason for limiting the mechanical properties of the alloy.

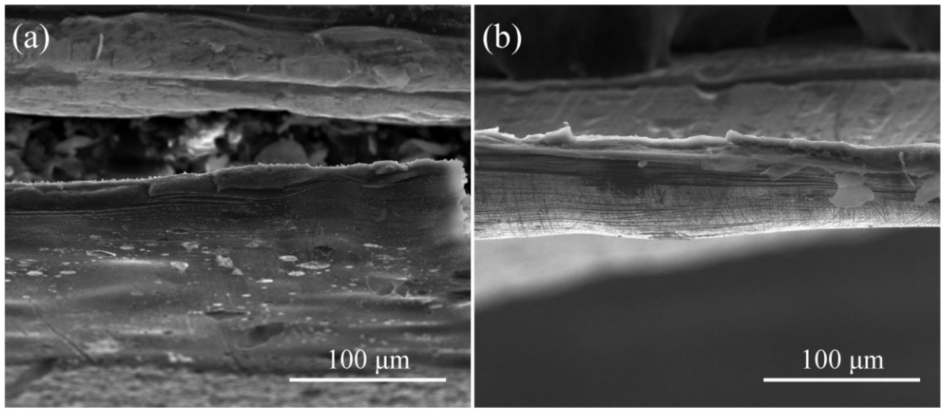

Figure 4. SEM images showing fracture of the magnesium-based amorphous alloy ribbons: (**a**) $Mg_{64}Zn_{30}Ce_6$ and (**b**) $Mg_{62}Zn_{30}Ce_8$.

SEM images showing the ribbon fracture morphology are presented in Figure 5. The dented morphology of the amorphous alloy sample was similar to that of other

previously reported amorphous alloys [29,30]. Dent size can be positively correlated with plasticity; therefore, the toughness of the $Mg_{68}Zn_{30}Ce_2$ sample was superior to that of the $Mg_{66}Zn_{30}Ce_4$ sample, which was consistent with the actual results.

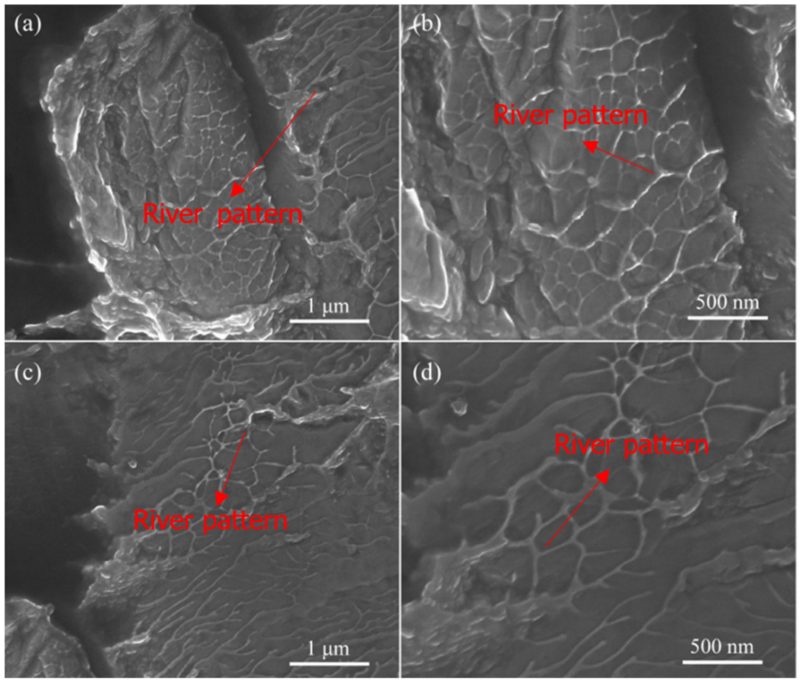

Figure 5. SEM images showing fracture of the magnesium-based amorphous alloy ribbons: (**a**,**b**) $Mg_{68}Zn_{30}Ce_2$, (**c**,**d**) $Mg_{66}Zn_{30}Ce_4$.

SEM images showing the bending fracture of the ribbons are presented in Figure 6, where the creases of the ribbon bending could be clearly seen. Dense shear bands appeared on both sides of the crease in the amorphous alloy ribbons. The distribution of shear bands in the $Mg_{68}Zn_{30}Ce_2$ amorphous ribbon was denser than in the $Mg_{66}Zn_{30}Ce_4$ amorphous ribbon; therefore, the $Mg_{68}Zn_{30}Ce_2$ sample had superior toughness compared to the $Mg_{66}Zn_{30}Ce_4$ sample. The propagation of the shear band at the fracture site in the $Mg_{66}Zn_{30}Ce_4$ amorphous ribbon was more prominent, and growth morphology of the shear bands resembling a vein pattern was observed, possibly due to the energy released during the fracture process [31]. Further magnification revealed densely distributed corrugated patterns and dents of different sizes in the shear bands. In addition, the sizes of the dents increased proportionally to the distance from the crease (close to the surface).

A schematic diagram for fracture in the amorphous ribbons is shown in Figure 7, according to the experimentally obtained microscopic fracture morphologies in the amorphous ribbons. As shown in Figure 7b, the crack originated at point Q and extended along the shear band in the QA, QB, or QC directions, depending on the specific microstructure of the sample at point Q and the direction in which the energy was most quickly released. The crack continued to extend until the amorphous ribbon was eventually broken. As shown by Figure 7d, crack extension during the fracture process of the sample was uncertain. The crack size was larger in the ductile shear band; therefore, the dent size was also larger. As the transition from the ductile shear band to the brittle shear band accelerated, the cracks became smaller but denser. The sizes of the dents also started to decrease with rapid breaking of the ribbon, ending the propagation of the shear band.

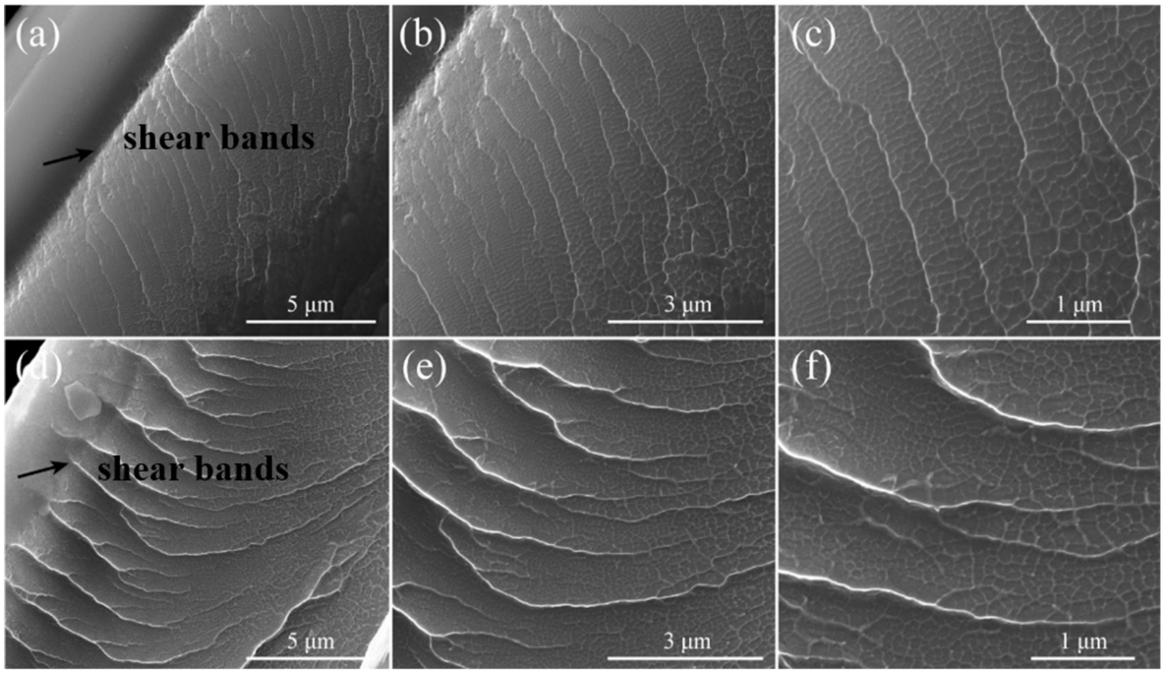

Figure 6. SEM images showing bending fracture of the magnesium-based amorphous alloy ribbon samples: (**a**–**c**) $Mg_{68}Zn_{30}Ce_2$, (**d**–**f**) $Mg_{66}Zn_{30}Ce_4$.

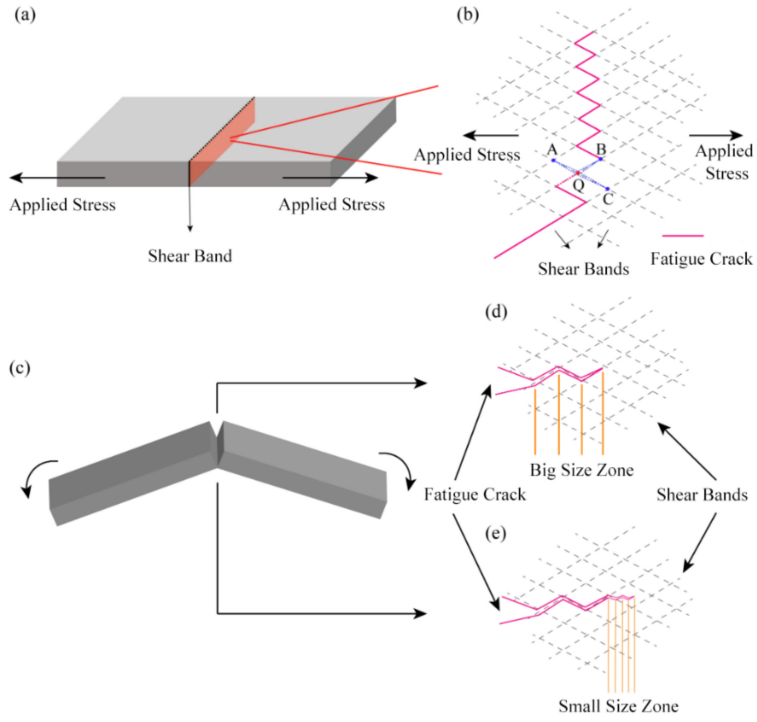

Figure 7. Fracture schematic diagram of the $Mg_{70-x}Zn_{30}Ce_x$ (x = 2, 4, 6 and 8 at.%) amorphous ribbon samples: (**a**) 3D schematic diagram of the ribbon stretching, (**b**) microscopic schematic diagram, (**c**) 3D schematic diagram of ribbon bending, (**d**,**e**) microscopic schematic diagrams of bending.

3.4. Electrochemical Properties

3.4.1. Open Circuit Potential and Polarization Curve Analysis

Because Ce (−2.34 V) and Zn (−0.76 V) have higher standard hydrogen electrode potentials than Mg (−2.37 V), the addition of these two elements would raise the corrosion

potential value. Figure 8a shows the OCP and polarization curves of the samples tested in SBF solution. When the Ce content was x = 2, 4 and 6, the OCP values of the samples were similar. The highest OCP value occurred at x = 6 and the lowest at x = 8, indicating that excessive Ce reduced the sample OCP value.

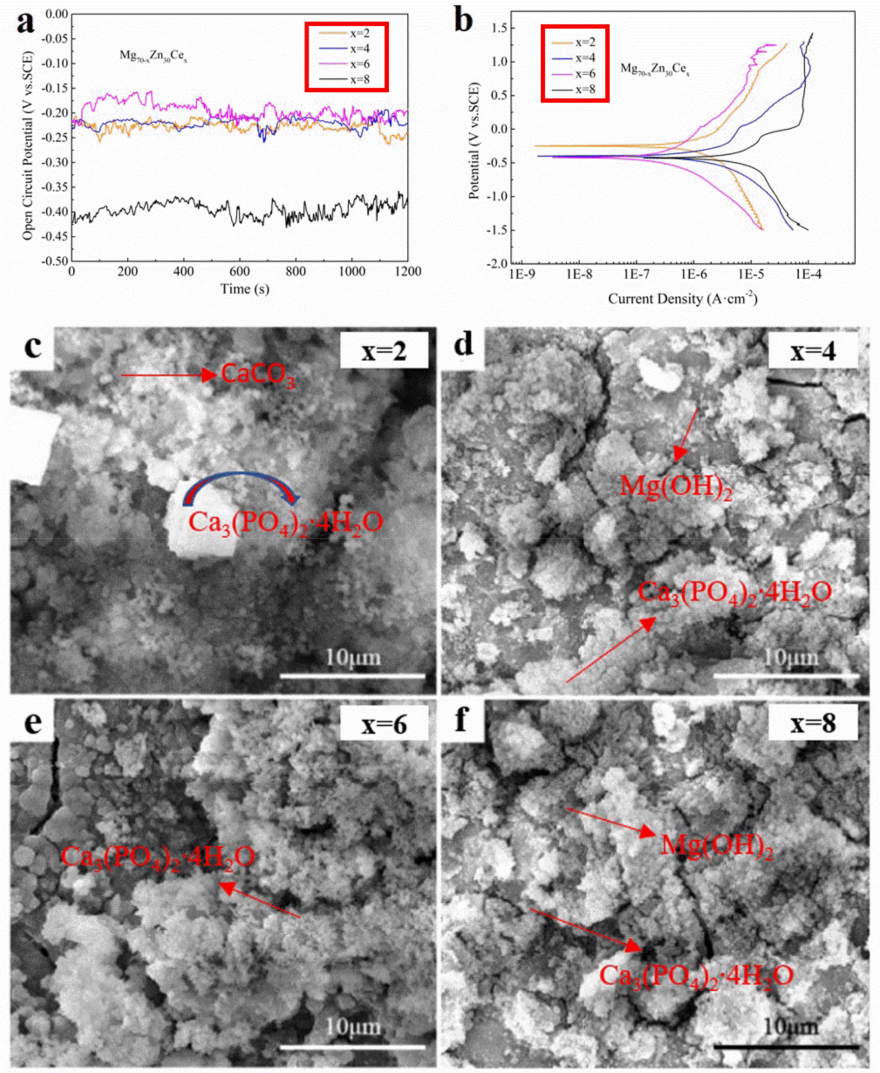

Figure 8. (**a**) OCP curves of $Mg_{70-x}Zn_{30}Ce_x$ (x = 2, 4, 6 and 8), and (**b**) polarization curves of $Mg_{70-x}Zn_{30}Ce_x$ (x = 2, 4, 6 and 8). Surface morphologies of the $Mg_{70-x}Zn_{30}Ce_x$ (x = 2, 4, 6, and 8) amorphous alloy samples after immersion in SBF for three days: (**c**) $Mg_{68}Zn_{30}Ce_2$, (**d**) $Mg_{66}Zn_{30}Ce_4$, (**e**) $Mg_{64}Zn_{30}Ce_6$, and (**f**) $Mg_{62}Zn_{30}Ce_8$.

In the polarization curve, the cathode side was controlled by the hydrogen evolution reaction, while the other side contained the anode dissolution reaction (i.e., the dissolution of Mg) and anodic hydrogen evolution (i.e., the negative difference effect) [32,33]. The cathodic reaction of the sample showed a passivation tendency with a lower potential than the breakdown potential, indicating the presence of an oxide film on the surface [34]. As shown in Figure 8b, the corrosion current density of $Mg_{64}Zn_{30}Ce_6$ was the lowest, while that of $Mg_{62}Zn_{30}Ce_8$ was the highest. When the Ce content was x = 4 and 6, the curve had an obvious Z shape, indicating that the corrosion products that formed on the sample surface protected the sample surface and slowed down the dissolution rate. Therefore, formation of the passivation layer effectively delayed the corrosion process. The results also showed that the $Mg_{64}Zn_{30}Ce_6$ magnesium-based amorphous alloy had the best corrosion

resistance, while the $Mg_{62}Zn_{30}Ce_8$ alloy had the lowest corrosion resistance. Furthermore, with the addition of Ce, the corrosion resistance deteriorated.

3.4.2. Electrochemical Impedance Analysis

The EIS test results and impedance equivalent circuit diagram of the $Mg_{70-x}Zn_{30}Ce_x$ sample (x = 2, 4, 6, and 8) are shown in Figure 4. Figure 9a shows the Nyquist diagram with two capacitive loops at high and intermediate frequencies. The diameter of the high-frequency capacitive reactance loop of $Mg_{64}Zn_{30}Ce_6$ was the largest, followed by $Mg_{66}Zn_{30}Ce4$, while the capacitive reactance loops of $Mg_{68}Zn_{30}Ce_2$ and $Mg_{62}Zn_{30}Ce_8$ were smaller in diameter, indicating that both reduced and excessive addition of Ce lowered the charge-transfer resistance of the amorphous alloy [35]. Additionally, the shapes of the high and intermediate frequency capacitive reactance loops of the $Mg_{68}Zn_{30}Ce_2$ sample were clearly distinguishable, possibly due to the relatively smooth surface of $Mg_{68}Zn_{30}Ce_2$, resulting in a different diffusion process during corrosion compared to the other samples [36]. The Bode diagrams of the samples are shown in Figure 9b,c. In the Bode diagram for |Z| and frequency, the resistance value of $Mg_{64}Zn_{30}Ce_6$ was the highest, whereas the resistance values of $Mg_{68}Zn_{30}Ce_2$ and $Mg_{62}Zn_{30}Ce_8$ were lower, indicating that adequate addition of Ce could help to alleviate damage to the passivation layer on the sample surface.

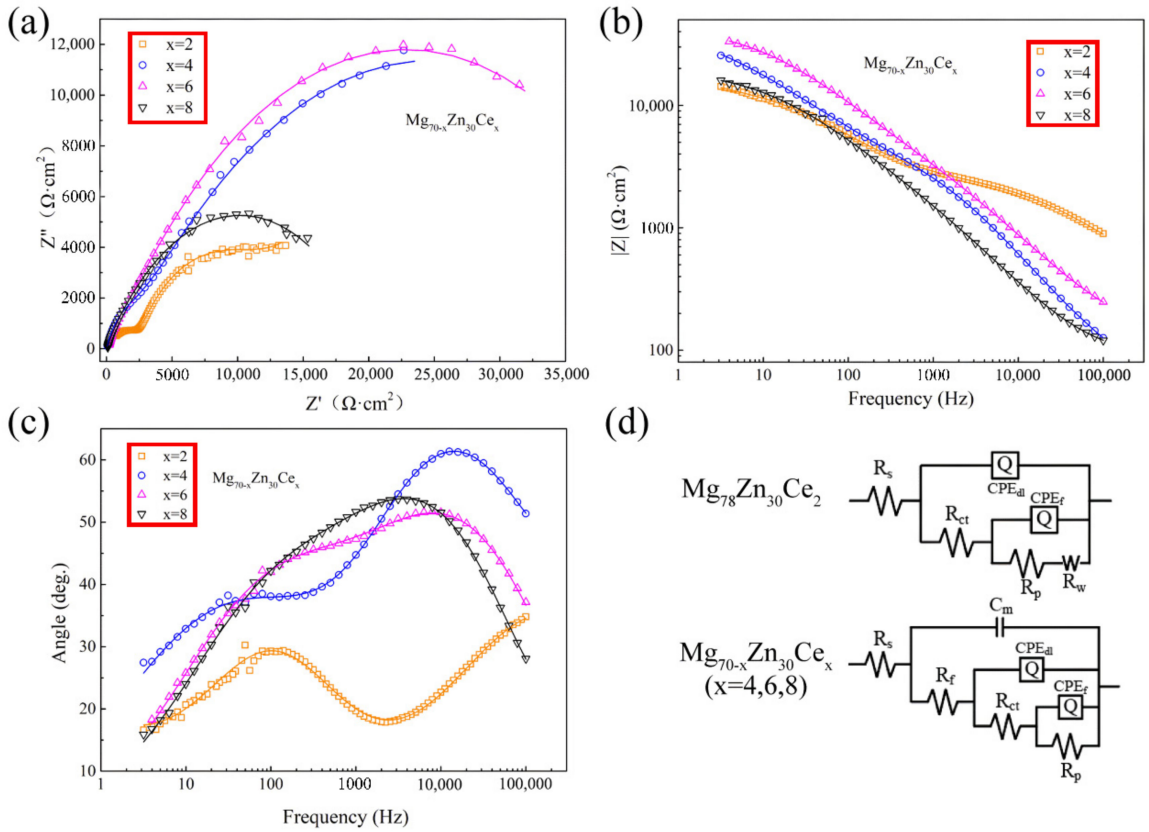

Figure 9. (**a**) Nyquist curves of the $Mg_{70-x}Zn_{30}Ce_x$ (x = 2, 4, 6, and 8) amorphous alloys, (**b**,**c**) Bode curves of the $Mg_{70-x}Zn_{30}Ce_x$ (x = 2, 4, 6, and 8) amorphous alloys, (**d**) equivalent circuit diagrams of the $Mg_{70-x}Zn_{30}Ce_x$ (x = 2, 4, 6, and 8) amorphous alloys.

ZSimDemo software (3.2, AMETEK, Inc., Berwyn, PA, USA) was used to fit the equivalent circuit diagram shown in Figure 9a, combined with more information obtained from the EIS test results. The fitting results are listed in Tables 2 and 3, where R_s is the solution resistance, and CPE_f and CPE_{dl} (constant phase element) represent the capacitance of the corrosion product film and the double-layer capacitance at the interface between the metal substrate and the electrolyte solution, respectively. Additionally, the value of n was

related to the surface roughness and the unevenness caused by the corrosion process. The constant phase element (CPE), which solves the deviation of dielectric properties, can be substituted for capacitors for better fitting analysis [37]. The CPE specifies that a resistor will have an n value that is equal to 0, while for a capacitor, n will be equal to 1.

Table 2. The first part fitting results for each component in the equivalent circuit diagram.

Sample	R_{ct} ($\Omega \cdot cm^2$)	Y_f ($\Omega^{-1} \cdot cm^{-2} \cdot s^{-1}$)	n_f	R_p ($\Omega \cdot cm^2$)	Z_w ($\Omega \cdot cm^2$)
$Mg_{68}Zn_{30}Ce_2$	2630	1.90×10^{-6}	0.72	1.03×10^4	5.90×10^{-5}
$Mg_{66}Zn_{30}Ce_4$	3297	4.25×10^{-6}	0.57	4.44×10^4	-
$Mg_{64}Zn_{30}Ce_6$	5093	1.37×10^{-6}	0.59	3.95×10^4	-
$Mg_{62}Zn_{30}Ce_8$	2841	3.50×10^{-6}	0.56	1.73×10^4	-

Table 3. The second part fitting results for each component in the equivalent circuit diagram.

Sample	R_s ($\Omega \cdot cm^2$)	C_m ($F \cdot cm^{-2}$)	R_f ($\Omega \cdot cm^2$)	Y_{dl} ($\Omega^{-1} \cdot cm^{-2} \cdot s^{-1}$)	n_{dl}
$Mg_{68}Zn_{30}Ce_2$	155.30	-	-	3.14×10^{-7}	0.60
$Mg_{66}Zn_{30}Ce_4$	36.65	8.83×10^{-9}	110.31	2.13×10^{-7}	0.78
$Mg_{64}Zn_{30}Ce_6$	123.90	8.12×10^{-21}	0.02	3.91×10^{-7}	0.80
$Mg_{62}Zn_{30}Ce_8$	4.23	6.52×10^{-10}	84.61	6.77×10^{-7}	0.76

The EIS curve of the Mg-Zn-Ce amorphous alloy was fitted by the equivalent circuit diagram in Figure 9d. For $Mg_{68}Zn_{30}Ce_2$, Z_w specified that the diffusion processes were simultaneously present during electrochemical polarization and concentration polarization. Generally speaking, the higher the R_{ct} value, the better the corrosion resistance of the metal [38]. After comparing the R_{ct} values, the R_{ct} value of $Mg_{64}Zn_{30}Ce_6$ was the highest at 5093 $\Omega \cdot cm^2$, followed by $Mg_{66}Zn_{30}Ce_4$, while the R_{ct} values of $Mg_{68}Zn_{30}Ce_2$ and $Mg_{62}Zn_{30}Ce_8$ were smaller. The fitting results were consistent with the EIS curve results, indicating that adequate Ce content in the Mg-Zn-Ce amorphous alloy system could improve its corrosion resistance.

3.5. Analysis of the XPS Results

An SEM was used to observe sample surface morphology after immersion in simulated body fluid for three days, as shown in Figure 8. The surface of the $Mg_{70-x}Zn_{30}Ce_x$ (x = 2, 4, 6, and 8) amorphous alloy was covered with dense inorganic salts, which formed a passivation film that inhibited contact between the sample and the corrosion medium; thus, deferring the corrosion process.

To study the composition of the passivation film and the corrosion products on the alloy surface, the $Mg_{70-x}Zn_{30}Ce_x$ (x = 2, 4, 6, and 8) amorphous alloy ribbon samples that were immersed in SBF for three days were subjected to XPS testing, as shown in Figure 10.

The peaks for each element in the amorphous alloy sample, specifically O1s, Ca2p, Mg1s, and Zn2p, are shown in the XPS spectrum in Figure 11. The 347 eV Ca2p peak indicated the formation of calcium carbonate in the passivation film, and the peak at 352 eV indicated the presence of calcium phosphate compounds and magnesium ions in the passivation film. The peaks of Ca2p at 350.8 eV and P2p at 133 eV indicated the presence of calcium phosphate in the corrosion products, and the peak position shifts for the different compositions were possibly associated with specific components, such as chlorapatite and hydroxyapatite [39]. In addition, binding energies of Mg1s at 1304 and 1303.5 eV represented $Mg(OH)_2$ and MgO in the corrosion products, respectively [40]. The presence of the aforementioned compounds was verified by O1s peaks at various positions, and the H_2O peak at 533 eV indicated the presence of water from crystallization in the corrosion products [41]. The Zn2p peak indicated that Zn on the sample surface was mainly in the form of pure metal [42].

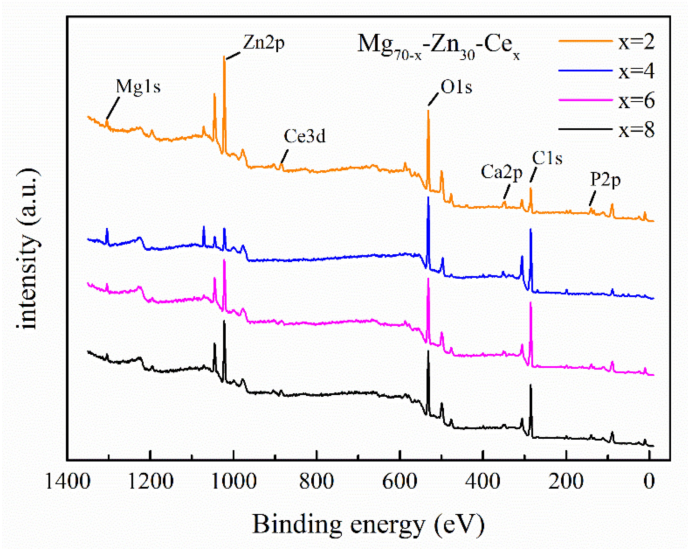

Figure 10. XPS spectra of the $Mg_{70-x}Zn_{30}Ce_x$ (x = 2, 4, 6 and 8) amorphous alloy ribbons after corrosion.

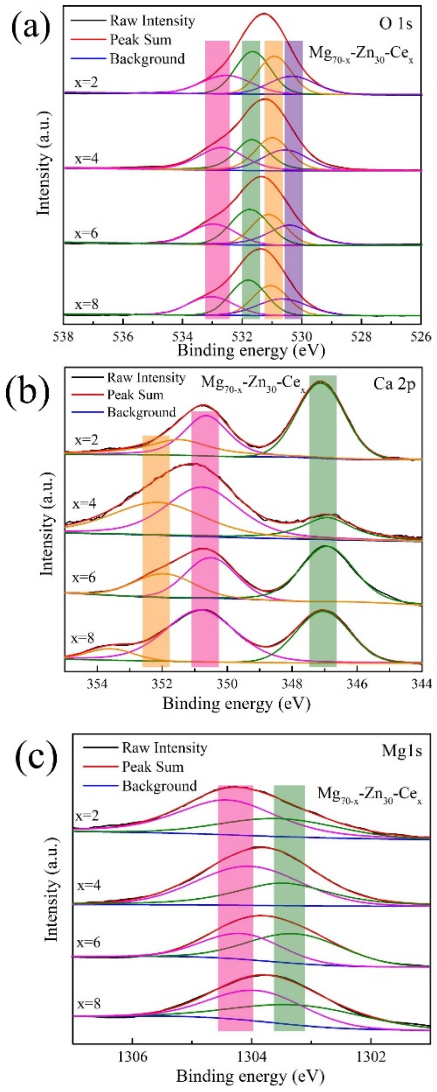

Figure 11. *Cont*.

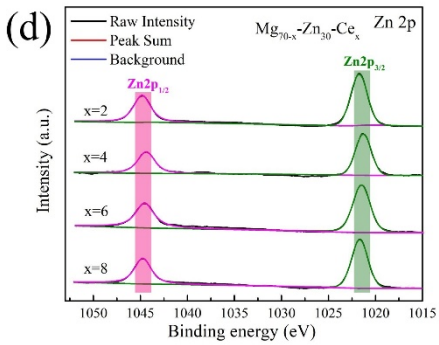

Figure 11. (**a**–**d**) Peak fitting curves for the XPS spectra of O1s, Ca2p, Mg1s, and Zn2p in the $Mg_{70-x}Zn_{30}Ce_x$ (x = 2, 4, 6, and 8) amorphous alloys, respectively.

As shown in Figure 12, multiple Ce3d peaks were observed. The characteristic peaks marked with u and v belonged to the 3d3/2 and 3d5/2 orbitals of Ce. The characteristic peaks of Ce^{4+} correlated to u_0, u_1, u_3, v_0, v_1, v_2, and v_4, while the characteristic peaks of Ce^{3+} correlated to u_2, u_4, v_3, and v_5 [43].Ce is relatively active; therefore, it likely preferentially reacted with dissolved oxygen in the simulated body fluid. Thus, Ce^{4+} was present in the form of CeO_2, whereas Ce^{3+} was likely in the form of Ce_2O_3. The solubility product constants of the phosphates followed the order: $Ca_3(PO_4)_2$ ($Ksp = 2.07 \times 10^{-33}$) < $Zn_3(PO_4)_2$ ($Ksp = 9.1 \times 10^{-33}$) < $Mg_3(PO_4)_2$ ($Ksp = 1.04 \times 10^{-24}$) < $CePO_4$ ($Ksp = 7.43 \times 10^{-11}$) [42]. Calcium phosphate always remained in the final corrosion products, regardless of whether a Mg-based or Zn-based matrix was used, and zinc phosphate or magnesium phosphate converted to calcium phosphate based on the change in precipitation–dissolution equilibrium.

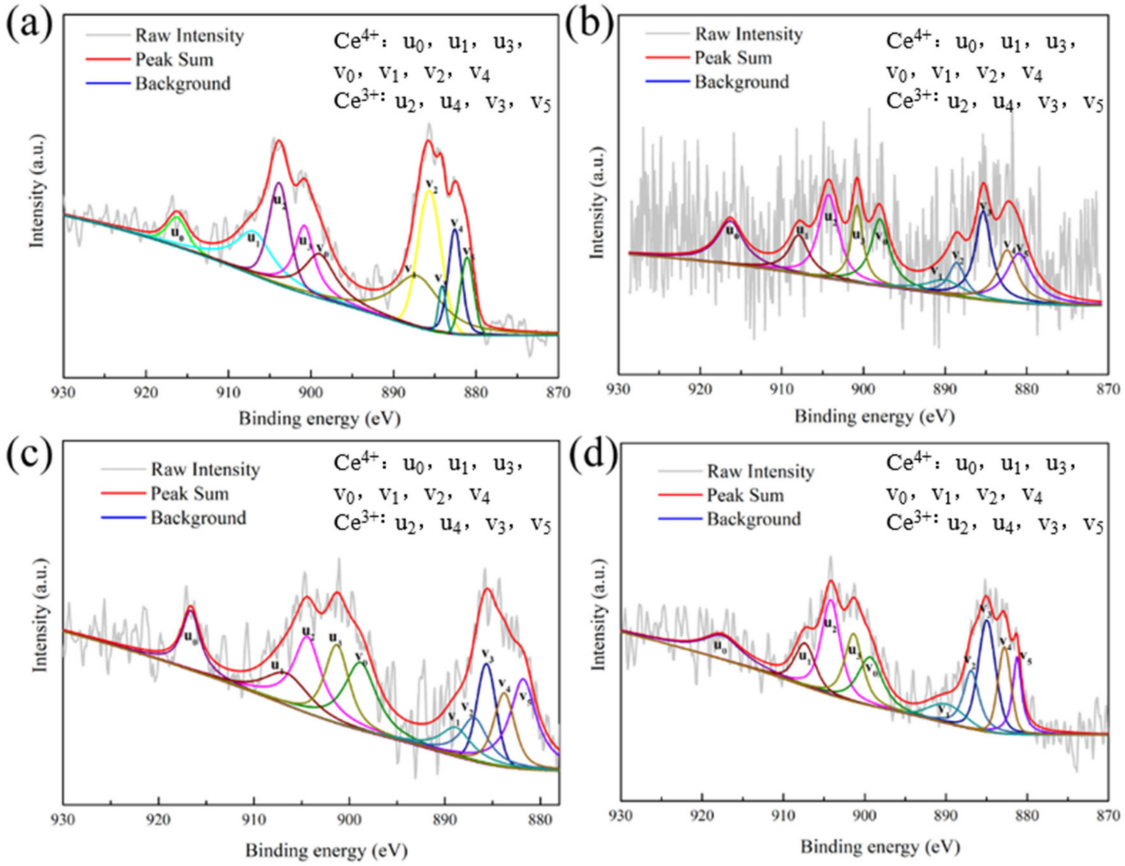

Figure 12. (**a**) Ce-2, (**b**) Ce-4, (**c**) Ce-6, and (**d**) Ce-8 peak fitting curves for the XPS spectra of the $Mg_{70-x}Zn_{30}Ce_x$ (x = 2, 4, 6 and 8) amorphous alloys.

3.6. Corrosion Behavior of Mg-Zn-Ce Amorphous Alloy

The corrosion products from the amorphous alloy in the simulated body fluid were assessed by XPS spectrum analysis, which in turn identified the corrosion mechanism of the amorphous alloy. The chemical reactions were summarized as follows:

Anodic reaction:

$$Mg \rightarrow Mg^{2+} + e^{2-},$$

$$Ce \rightarrow Ce^{3+} + 3e^{-},$$

$$Ce \rightarrow Ce^{4+} + 4e^{-},$$

and cathodic reaction:

$$2H_2O + 2e^{2-} \rightarrow 2OH^{-} + H_2\uparrow$$

Eventually, a passivation film formed on the surface of the amorphous alloy ribbons, delaying the corrosion process of the amorphous alloys. The reactions followed:

$$Mg^{2+} + 2OH^{-} \rightarrow Mg(OH)_2,$$

$$2Mg + O_2 \rightarrow 2MgO,$$

$$Ce + O_2 \rightarrow CeO_2,$$

$$2Ce + 3O_2 \rightarrow 2Ce_2O_3.$$

The surface hydrolysis reaction would continue, and the passivation film would break down and recover. Thus, a stable passivation film provided support for the slow and controllable degradation of the material, according to:

$$Ca^{2+} + CO_3{}^{2-} \rightarrow CaCO_3,$$

$$H_2PO_4{}^{-} + OH^{-} \rightarrow HPO_4{}^{2-} + H_2O,$$

$$HPO_4{}^{2-} + OH^{-} \rightarrow PO_4{}^{3-} + H_2O,$$

$$3Ca^{2+} + 2H_2PO_4{}^{-} + 4OH^{-} \rightarrow Ca_3(PO_4)_2{\cdot}4H_2O,$$

$$Mg^{2+} + Ca^{2+} + HPO_4{}^{2-} + OH^{-} \rightarrow xMg^{2+}\text{-}yCa_3(PO_4)_2{\cdot}zH_2O.$$

A schematic diagram depicting the degradation of the Mg-Zn-Ce amorphous alloy is shown in Figure 13. The metal ions and the solution ions underwent physical and chemical reactions on the surface of the ribbon, eventually producing $Mg(OH)_2$, $CaCO_3$, $Ca_3(PO_4)_2{\cdot}4H_2O$, and calcium phosphate compounds and magnesium ions. As a result, the formation of a dense $Ca_3(PO_4)_2{\cdot}4H_2O$ film could effectively alleviate the hydrolysis process of $Mg(OH)_2$ and the metal matrix, thus slowing down the corrosion of the sample.

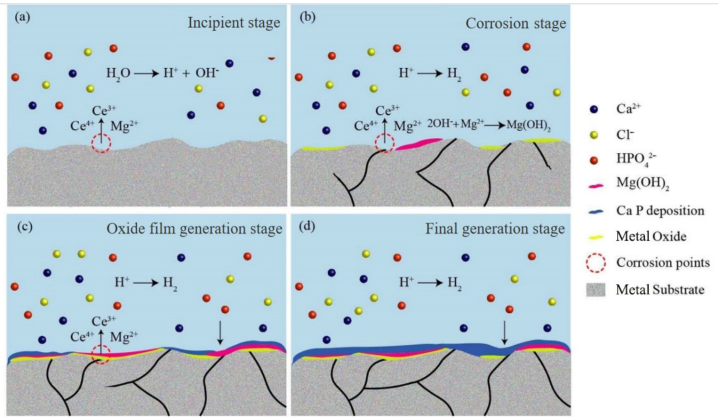

Figure 13. Schematic diagram showing the corrosion of the magnesium-based amorphous alloy immersed in SBF. (**a**–**d**) Representation of the gradual corrosion progress.

4. Conclusions

(1) XRD and DSC results verified the amorphous structures of the $Mg_{70-x}Zn_{30}Ce_x$ (x = 2, 4, 6, and 8) alloys.
(2) The elastic modulus of the $Mg_{70-x}Zn_{30}Ce_x$ (x = 2, 4, 6, and 8) amorphous alloy was similar to that of human bone, and it could effectively avoid the resulting stress shielding effect if the material was used as a bone implant.
(3) In the simulated body fluid, the $Mg_{64}Zn_{30}Ce_6$ sample had the best corrosion resistance, followed by $Mg_{66}Zn_{30}Ce_4$.
(4) Ce in the sample would preferentially react with the dissolved oxygen in the solution, forming Ce oxides (CeO_2 and Ce_2O_3). Insoluble oxides reduced the corrosion rate of the alloy, producing a dense $Ca_3(PO_4)_2 \cdot 4H_2O$ film in the subsequent reaction, which further delayed corrosion of the alloy.

The results showed that the addition of Ce endowed the Mg-Zn-Ce amorphous alloy with superior mechanical properties and decent corrosion resistance, thereby improving the potential for development and applications of the alloy.

Author Contributions: Conceptualization, M.H.; Data curation, M.W.; Formal analysis, K.Z.; Investigation, H.W.; Methodology, H.J.; Project administration, Z.L. All authors have read and agreed to the published version of the manuscript.

Funding: This research was funded by National Natural Science Foundation, China (Grant No. 51771120 and 51304136).

Data Availability Statement: Data presented in this study maybe requested from the corresponding author.

Acknowledgments: This study was supported by National Natural Science Foundation, China (Grant No. 51771120 and 51304136).

Conflicts of Interest: The authors declare no conflict of interest.

References

1. Wong, P.-C.; Tsai, P.-H.; Li, T.-H.; Cheng, C.-K.; Jang, J.; Huang, J. Degradation behavior and mechanical strength of Mg-Zn-Ca bulk metallic glass composites with Ti particles as biodegradable materials. *J. Alloys Compd.* **2017**, *699*, 914–920. [CrossRef]
2. Li, X.; Liu, X.; Wu, S.; Yeung, K.; Zheng, Y.; Chu, P.K. Design of magnesium alloys with controllable degradation for biomedical implants: From bulk to surface. *Acta Biomater.* **2016**, *45*, 2–30. [CrossRef] [PubMed]
3. Saini, M.; Singh, Y.; Arora, P.; Arora, V.; Jain, K. Implant biomaterials: A comprehensive review. *J. World J. Clin. Cases* **2015**, *31*, 52–57. [CrossRef]
4. Tong, X.; Zhang, D.C.; Zhang, X.T.; Su, Y.C.; Shi, Z.M.; Wang, K.; Lin, J.G.; Li, Y.C.; Lin, J.X.; Wen, C. Microstructure, mechanical properties, biocompatibility, and in vitro corrosion and degradation behavior of a new Zn-5Ge alloy for biodegradable implant materials. *J. Acta Biomater.* **2018**, *82*, 197–204. [CrossRef] [PubMed]
5. Jana, A.; Das, M.; Balla, V.K. Effect of heat treatment on microstructure, mechanical, corrosion and biocompatibility of Mg-Zn-Zr-Gd-Nd alloy. *J. Alloys Compd.* **2019**, *821*, 153462. [CrossRef]
6. Zhao, D.; Witte, F.; Lu, F.; Wang, J.; Li, J.; Qin, L. Current status on clinical applications of magnesium-based orthopaedic implants: A review from clinical translational perspective. *Biomaterials* **2017**, *112*, 287–302. [CrossRef]
7. Gu, X.; Xie, X.; Li, N.; Zheng, Y.; Qin, L. In vitro and in vivo studies on a Mg–Sr binary alloy system developed as a new kind of biodegradable metal. *Acta Biomater.* **2012**, *8*, 2360–2374. [CrossRef]
8. Lee, J.I.; Ryu, W.H.; Yoon, K.N.; Park, E.S. In-situ synthesis of Mg-based bulk metallic glass matrix composites with primary α-Mg phases. *J. Alloys Compd.* **2021**, *879*, 160417. [CrossRef]
9. Roche, V.; Koga, G.; Matias, T.; Kiminami, C.; Bolfarini, C.; Botta, W.; Nogueira, R.; Junior, A.J. Degradation of biodegradable implants: The influence of microstructure and composition of Mg-Zn-Ca alloys. *J. Alloys Compd.* **2018**, *774*, 168–181. [CrossRef]
10. Samiri, A.; Khmich, A.; Hassani, A.; Hasnaoui, A. Elastic and structural properties of $Mg_{25}Al_{75}$ binary metallic glass under different cooling conditions. *J. Alloys Compd.* **2021**, *891*, 161979. [CrossRef]
11. Wu, R.; Yan, Y.; Wang, G.; Murr, L.; Han, W.; Zhang, Z.; Zhang, M. Recent progress in magnesium–lithium alloys. *Int. Mater. Rev.* **2014**, *60*, 65–100. [CrossRef]
12. Ding, W.J. Opportunities and challenges for the biodegradable magnesium alloys as next-generation biomaterials. *J. Regen. Biomater.* **2016**, *32*, 79–86. [CrossRef] [PubMed]
13. Yin, J.; Ma, X.; Zhou, Z. Composition and size dependent brittle-to-malleable transitions of Mg-based bulk metallic glasses. *Mater. Sci. Eng. A* **2014**, *605*, 286–293. [CrossRef]

14. Zberg, B.; Uggowitzer, P.J.; Löffler, J.F. MgZnCa glasses without clinically observable hydrogen evolution for biodegradable implants. *Nat. Mater.* **2009**, *8*, 887–891. [CrossRef] [PubMed]
15. González, S.; Figueroa, I.; Todd, I. Influence of minor alloying additions on the glass-forming ability of Mg–Ni–La bulk metallic glasses. *J. Alloys Compd.* **2009**, *484*, 612–618. [CrossRef]
16. Chen, J.; Dong, J.; Fu, H.; Zhang, H.; Tan, L.; Zhao, D.; Yang, K. In vitro and in vivo studies on the biodegradable behavior and bone response of Mg69Zn27Ca4 metal glass for treatment of bone defect. *J. Mater. Sci. Technol.* **2019**, *35*, 2254–2262. [CrossRef]
17. Esmaily, M.; Svensson, J.E.; Fajardo, S.; Birbilis, N.; Frankel, G.S.; Virtanen, S.; Arrabal, R.; Thomas, S.; Johansson, L.G. Fundamentals and advances in magnesium alloy corrosion. *Prog. Mater. Sci.* **2017**, *89*, 92–193. [CrossRef]
18. Lei, X.; Wei, Y.; Wei, B.; Wang, W.-H. Spiral fracture in metallic glasses and its correlation with failure criterion. *Acta Mater.* **2015**, *99*, 206–212. [CrossRef]
19. Li, H.F.; Zheng, Y.F. Recent advances in bulk metallic glasses for biomedical applications. *Acta Biomater.* **2016**, *36*, 1–20. [CrossRef]
20. Li, K.; Liang, L.; Du, P.; Cai, Z.; Xiang, T.; Kanetaka, H.; Wu, H.; Xie, G. Mechanical properties and corrosion resistance of powder metallurgical Mg-Zn-Ca/Fe bulk metal glass composites for biomedical application. *J. Mater. Sci. Technol.* **2021**, *103*, 73–83. [CrossRef]
21. Liu, D.; Yang, D.; Li, X.; Hu, S. Mechanical properties, corrosion resistance and biocompatibilities of degradable Mg-RE alloys: A review. *J. Mater. Res. Technol.* **2018**, *8*, 1538–1549. [CrossRef]
22. Ruan, Y.; Li, C.; Ren, Y.; Wu, X.; Schmid-Fetzer, R.; Guo, C.; Du, Z. Phases equilibrated with long-period stacking ordered phases in the Mg-rich corner of the Mg-Y-Zn system. *J. Mater. Sci. Technol.* **2020**, *68*, 147–159. [CrossRef]
23. Pan, D.G.; Liu, W.Y.; Zhang, H.F.; Wang, A.M.; Hu, Z.Q. Mg–Cu–Ag–Gd–Ni bulk metallic glass with high mechanical strength. *J. Alloys Compd.* **2007**, *438*, 142–144. [CrossRef]
24. Willbold, E.; Gu, X.N.; Albert, D.; Kalla, K.; Bobe, K.; Brauneis, M.; Janning, C.; Nellesen, J.; Czayka, W.; Tillmann, W.; et al. Effect of the addition of low rare earth elements (lanthanum, neodymium, cerium) on the biodegradation and biocompatibility of magnesium. *J. Acta Biomater.* **2015**, *11*, 554–562. [CrossRef] [PubMed]
25. Shen, L.Q.; Luo, P.; Hu, Y.C.; Bai, H.Y.; Sun, Y.H.; Sun, B.A.; Liu, Y.H.; Wang, W.H. Shear-band affected zone revealed by magnetic domains in a ferromagnetic metallic glass. *Nat. Commun.* **2018**, *9*, 1–9. [CrossRef] [PubMed]
26. Hufnagel, T.C.; Ott, R.; Almer, J. Structural aspects of elastic deformation of a metallic glass. *Phys. Rev. B* **2006**, *73*, 064204. [CrossRef]
27. Liu, Y.H.; Wang, G.; Wang, R.J.; Zhao, D.Q.; Pan, M.X.; Wang, W.H. Super Plastic Bulk Metallic Glasses at Room Temperature. *Science* **2007**, *315*, 1385–1388. [CrossRef]
28. Guo, W.; Kato, H.; Lü, S.; Wu, S. Porous NiTi Particle Dispersed Mg-Zn-Ca Bulk Metallic Glass Matrix Composites. *Materials* **2018**, *11*, 1959. [CrossRef]
29. Suh, J.-Y.; Conner, R.D.; Kim, C.P.; Demetriou, M.D.; Johnson, W.L. Correlation between fracture surface morphology and toughness in Zr-based bulk metallic glasses. *J. Mater. Res.* **2010**, *25*, 982–990. [CrossRef]
30. Qu, R.; Wang, S.; Li, G.; Wang, R.; Wang, X.; Wu, S.; Zhang, Z. Shear band fracture in metallic glass: Hot or cold? *Scr. Mater.* **2018**, *162*, 136–140. [CrossRef]
31. Liu, G.B.; Gao, P.; Xue, Z.; Yang, S.Q.; Zhang, M.L. Study on the formation of new Mg-Cu-Ti-Y quaternary bulk metallic glasses with high mechanical strength. *J. Non-Cryst. Solids* **2012**, *35823*, 3084–3088. [CrossRef]
32. Greer, A.L. Metallic glasses . . . on the threshold. *J. Mater. Today* **2009**, *12*, 14–22. [CrossRef]
33. Zeng, F.; Jiang, M.Q.; Dai, L.H. Dilatancy induced ductile-brittle transition of shear band in metallic glasses. *J. Proc. R. Soc. A-Math. Phys. Eng. Sci.* **2018**, *A474*, 20170836. [CrossRef] [PubMed]
34. Wang, G.; Liaw, P.K.; Jin, X.; Yokoyama, Y.; Huang, E.-W.; Jiang, F.; Keer, L.M.; Inoue, A. Fatigue initiation and propagation behavior in bulk-metallic glasses under a bending load. *J. Appl. Phys.* **2010**, *108*, 113512. [CrossRef]
35. Li, Z.; Song, G.-L.; Song, S. Effect of bicarbonate on biodegradation behaviour of pure magnesium in a simulated body fluid. *Electrochim. Acta* **2014**, *115*, 56–65. [CrossRef]
36. Cao, F.Y.; Shi, Z.M.; Song, G.L.; Liu, M.; Atrens, A. Corrosion behaviour in salt spray and in 3.5% NaCl solution saturated with Mg(OH)(2) of as-cast and solution heat-treated binary Mg-X alloys: X = Mn, Sn, Ca, Zn, Al, Zr, Si, Sr. *J. Corros. Sci.* **2013**, *76*, 60–97. [CrossRef]
37. Kumar, V.; Gupta, A.; Lahiri, D.; Balani, K. Serrated yielding during nanoindentation of thermomechanically processed novel Mg-9Li-7Al-1Sn and Mg-9Li-5Al-3Sn-1Zn alloys. *J. Phys. D-Appl. Phys.* **2013**, *46*, 145304. [CrossRef]
38. Liu, Q.; Ma, Q.-X.; Chen, G.-Q.; Cao, X.; Zhang, S.; Pan, J.-L.; Zhang, G.; Shi, Q.-Y. Enhanced corrosion resistance of AZ91 magnesium alloy through refinement and homogenization of surface microstructure by friction stir processing. *Corros. Sci.* **2018**, *138*, 284–296. [CrossRef]
39. Pan, H.; Pang, K.; Cui, F.; Ge, F.; Man, C.; Wang, X.; Cui, Z. Effect of alloyed Sr on the microstructure and corrosion behavior of biodegradable Mg-Zn-Mn alloy in Hanks' solution. *Corros. Sci.* **2019**, *157*, 420–437. [CrossRef]
40. Wang, B.; Xu, D.; Dong, J.; Ke, W. Effect of corrosion product films on the in vitro degradation behavior of Mg-3%Al-1%Zn (in wt%) alloy in Hank's solution. *J. Mater. Sci. Technol.* **2018**, *34*, 1756–1764.
41. Liu, Y.; Liu, X.; Zhang, Z.C.; Farrell, N.; Chen, D.F.; Zheng, Y.F. Comparative, real-time in situ monitoring of galvanic corrosion in Mg-Mg_2Ca and Mg-$MgZn_2$ couples in Hank's solution. *J. Corros. Sci.* **2019**, *161*, 108185. [CrossRef]

42. Wang, Y.; Tan, M.J.; Pang, J.; Wang, Z.; Jarfors, A.W. In vitro corrosion behaviors of $Mg_{67}Zn_{28}Ca_5$ alloy: From amorphous to crystalline. *Mater. Chem. Phys.* **2012**, *134*, 1079–1087. [CrossRef]
43. Zhang, F.; Wang, P.; Koberstein, J.; Khalid, S.; Chan, S.W. Cerium oxidation state in ceria nanoparticles studied with X-ray pho-toelectron spectroscopy and absorption near edge spectroscopy. *J. Surf. Sci.* **2004**, *563*, 74–82. [CrossRef]